

The soft-mode phonons mediated unconventional superconductivity in monolayer 1T'-WTe₂

Wei Yang,¹ Chong-jie Mo,² Shi-Bin Fu,¹ Yu Yang,³ Fa-Wei Zheng,³
Xiao-Hui Wang,¹ Yuan-An Liu,¹ Ning Hao,^{4,*} and Ping Zhang^{3,5,2,†}

¹*Beijing Key Laboratory of Work Safety Intelligent Monitoring,
Beijing University of Posts and Telecommunications, Beijing 100876, China*

²*Beijing Computational Science Research Center, Beijing 100193, China*

³*Institute of Applied Physics and Computational Mathematics, Beijing 100088, China*

⁴*Anhui Province Key Laboratory of Condensed Matter Physics at Extreme Conditions,
High Magnetic Field Laboratory, HFIPS,
Chinese Academy of Sciences, Hefei, 230031, China*

⁵*School of Physics and Physical Engineering,
Qufu Normal University, Qufu 273165, China*

Abstract

Recent experiments have tuned the monolayer 1T'-WTe₂ to be superconducting by electrostatic gating. Here, we theoretically study the phonon-mediated superconductivity in monolayer 1T'-WTe₂ via charge doping. We reveal that the emergence of soft-mode phonons with specific momentum is crucial to give rise to the superconductivity in electron-doping regime, whereas no such soft-mode phonons and no superconductivity emerge in hole-doping regime. We also find a superconducting dome, which can be attributed to the change of Fermi surface nesting condition as electron doping. By taking into account the experimentally established strong anisotropy of temperature-dependent upper critical field H_{c2} between the in-plane and out-of-plane directions, we show that the superconducting state probably has the unconventional equal-spin-triplet pairing in A_u channel of C_{2h} point group. Our studies provide a promising understanding to the doping dependent superconductivity and strong anisotropy of H_{c2} in monolayer 1T'-WTe₂, and can be extended to understand the superconductivity in other gated transition metal dichalcogenides.

*Electronic address: haon@hmfll.ac.cn

†Electronic address: zhang_ping@iapcm.ac.cn

Tuning the topological materials to be superconducting provides a highly efficient way to search and study the exotic superconductivity such as unconventional and topological superconductivity. Some methods have been developed to achieve the target, including the doping through metal intercalation [1–4], high pressure [5, 6], proximity effect [7–10], hard and soft tip contact [11–15], and electrostatic gating [16, 17]. Among them, the electrostatic gating has advantage to freely tune the materials in both electron- and hole-doped regimes without introducing dopant. Recently, the intrinsic superconductivity in the monolayer topological insulator 1T'-WTe₂ have been experimentally observed by two groups through moderate electrostatic gating [16, 17]. It is found that the superconductivity shows some interesting features. For instance, only the electron-doped regime show the superconductivity with the transition temperature (T_c) up to 1 K, whereas no superconducting signature is observed in the hole-doped regime. Furthermore, the upper critical field H_{c2} shows strong anisotropy between the in-plane $H_{c2,\parallel}$ and out-of-plane $H_{c2,\perp}$, and $H_{c2,\parallel}$ is significantly larger and four times the Pauli paramagnetic limit $1.84T_c$. However, the gating-dependent superconductivity and the H_{c2} anisotropy have not been comprehensively understood.

In this work, we show that the phonon spectrum of 1T'-WTe₂ dramatically softens in the electron-doped regime, but slightly stiffens in the hole-doped regime through density functional calculations. According to the phonon-mediated superconductivity theory, we reveal that the softening of the phonons with specific momentum in electron-doped regime is the driving force to give rise to the superconductivity. We also find an optimal electron-doped concentration, beyond which, the T_c becomes to decline in accompany with the latent charge density wave (CDW) instability. Furthermore, we reveal the evolution of superconductivity coincides with the change of Fermi surface nesting condition, and predict the CDW order is quasi-one dimensional commensurate with wave vector $q_{CDW}=(0, \pi/b)$ according to the electronic susceptibility. Thus, there exist a superconducting dome and a new CDW state in the phase diagram. Based on the symmetry classification and linearized gap equations, we find that all the superconducting pairing channels with specific irreducible representations (IRs) are degenerate without external magnetic field. However, only the pairing in A_u channel shows the experimentally observed reasonable anisotropy between $H_{c2,\parallel}$ and $H_{c2,\perp}$. This behavior indicates that the superconductivity in 1T'-WTe₂ probably has equal-spin-triplet pairing and belongs to unconventional type.

The first-principles calculations in this work are performed using the density functional

theory (DFT) and the density functional perturbation theory (DFPT)[18, 19]. We employed the QUANTUM ESPRESSO (QE) package[20] for the electronic structure and lattice dynamics including the phonon spectrum and electron-phonon coupling. The superconducting transition temperature T_c is calculated with the McMillan-Allen-Dynes formula[21] as implemented in the QE package[20]. The details of the calculation are presented in the supplementary materials (SM)[22].

The charge doping effect from the electrostatic gating is simulated by adding or removing electrons to the monolayer 1T'-WTe₂ with a compensating uniform charge background. The doped carrier concentrations per 1T'-WTe₂ is expressed as n (cm⁻²), with positive and negative values indicating electron and hole doping, respectively. Figure 1 shows the electronic structure of 1T'-WTe₂ from the first-principle calculations. The Fermi surfaces in Figs. 1 (c) and (d) correspond to the hole and electron doping with carrier concentrations $n_h = -9.5 \times 10^{13}$ cm⁻² and $n_e = 9.5 \times 10^{13}$ cm⁻², respectively. Around the Fermi level, the d orbitals of W and p orbitals of Te are dominated. Along $\Gamma - X$ line, there are two electron pockets labeled by K' and K in electron-doped case while only one hole pocket centered at Γ point in hole-doped case. The details of calculations are presented in Section I and II in SM.

The calculated phonon spectrum $\omega_{q,\nu}$ with wave vector q and mode index ν in electron-doped 1T'-WTe₂ is shown in Fig. 2(a). Remarkably, some phonon modes at specific wave vectors Q and Q_i with $i=1,2,3$ dramatically soften in comparison with the non-doped case shown in Fig. S4 (a) in SM. However, the phonon spectrum of hole doping slightly stiffens, as shown in Fig. S4(d) in SM. This distinctly opposite trend of the phonon modes between electron doping and hole doping is clearly demonstrated in Fig. 2(c). The softening of Q mode phonon is enhanced as electron doping density increases, and its frequency ω_Q turns to be negative when n_e crosses 10.3×10^{13} cm⁻², as shown in the inset in Fig. 2(c). It means some long-range order instability could emerge. In the present case, such instability is probably the CDW. Furthermore, the relevant atomic displacements for the Q mode phonon are mainly expressed as horizontal W-W stretching vibration and shear Te-Te tortuosing vibration, as shown in Fig. S5 in SM. These behaviors indicate the Q mode phonon has the longitudinal-wave feature. We have checked that the properties of all Q_i mode phonon are similar to those of the Q mode phonon.

The features of phonon spectrum in Fig. 2 imply that the soft mode phonons should

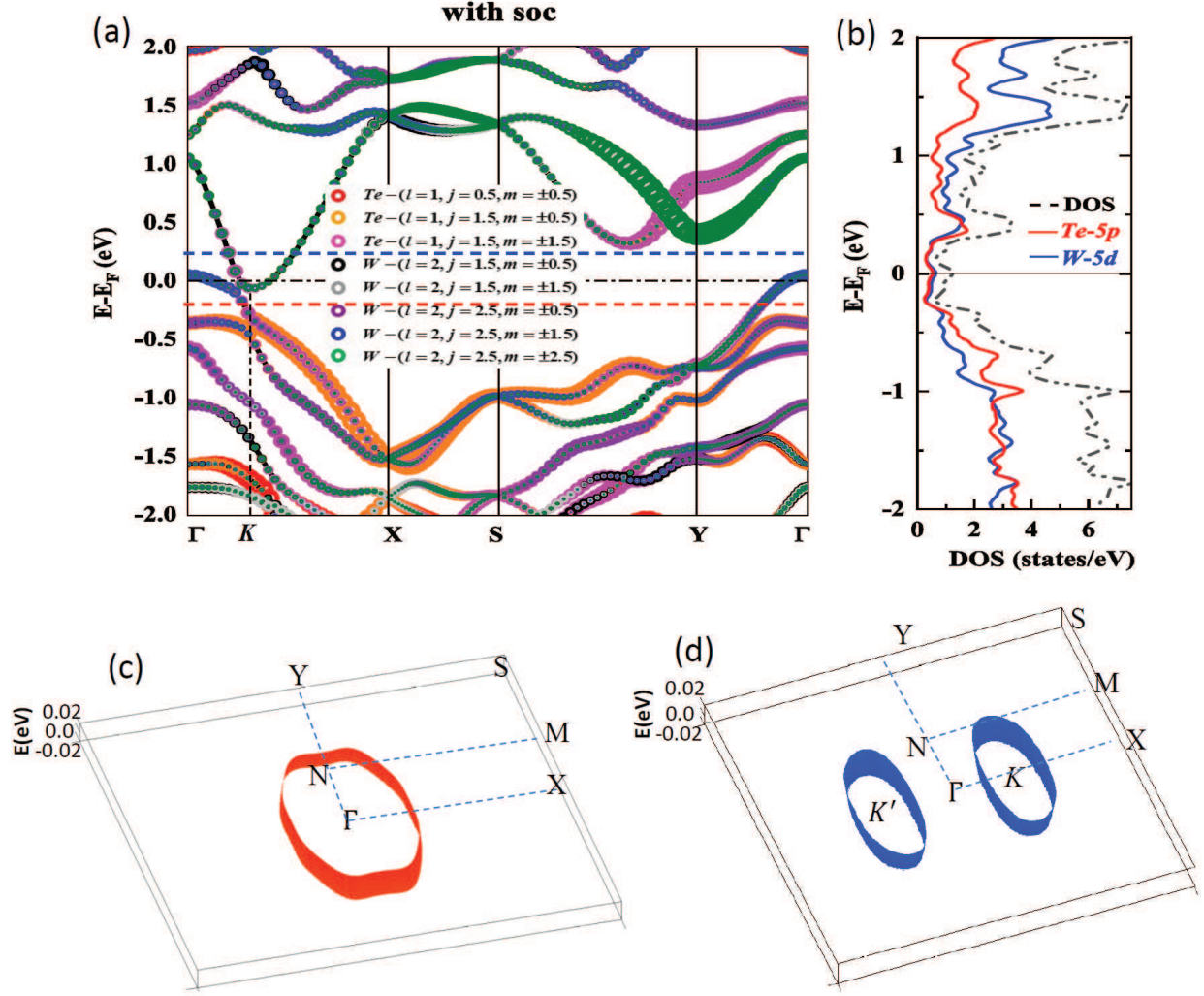


FIG. 1: (Color online)(a) The calculated orbital-resolved band structures of 1T'-WTe along the high-symmetry lines with spin-orbit coupling. The weight of the orbital is labeled by the linewidth. The conduction band bottom is labeled by $K = (0.17, 0)$ in units $\frac{2\pi}{a}$ and $\frac{2\pi}{b}$ ($a = 3.49\text{\AA}$ and $b = 6.31\text{\AA}$ are the lattice constants [25]). (b) The density of states of band structures in (a). (c) and (d) the Fermi surfaces for the hole doping with $n_h = -9.5 \times 10^{13} \text{ cm}^{-2}$ and electron doping with $n_e = 9.5 \times 10^{13} \text{ cm}^{-2}$, respectively. The plotting is set with energy window $[-0.02\text{eV}, 0.02\text{eV}]$. The Fermi levels with 0eV correspond to the red-dashed and blue-dashed lines in (a), respectively.

play a key role to induce the superconductivity in electron-doped monolayer 1T'-WTe₂. To prove it, we also plot the linewidth of the phonon spectrum $\gamma_{q,\nu}$ shown in Fig. 2(a), the Eliashberg spectral function $\alpha^2 F(\omega)$ and the frequency-dependent electron-phonon coupling

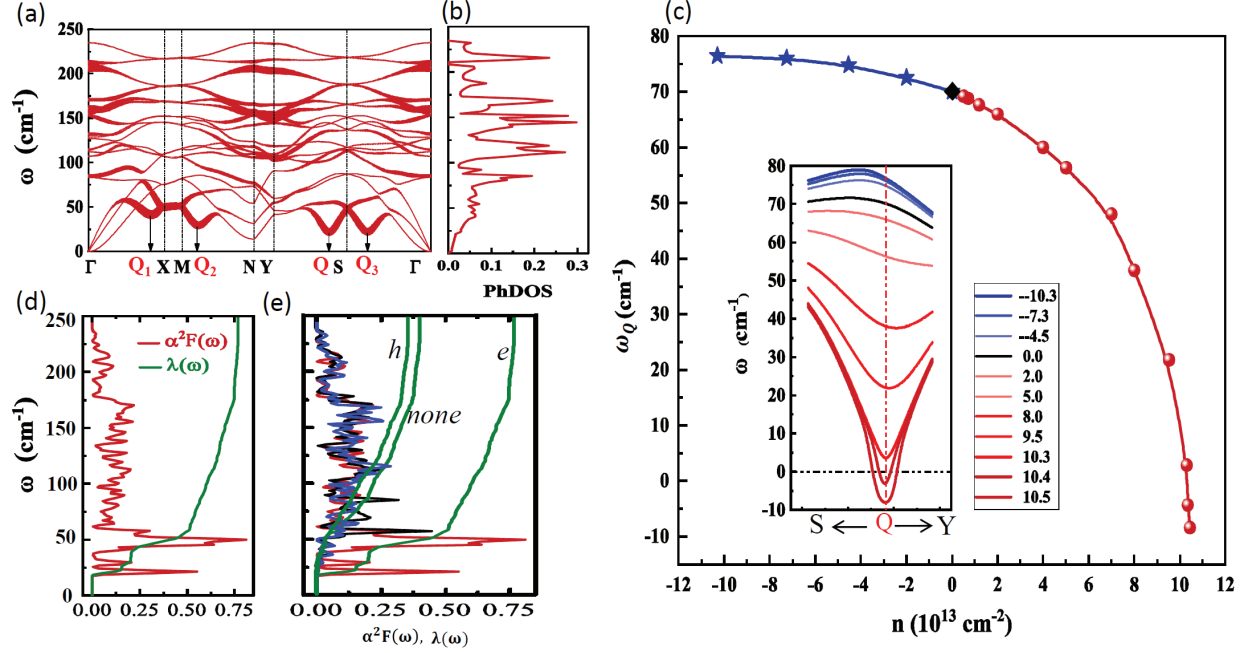


FIG. 2: (Color online) (a) The calculated phonon spectra for e -doped monolayer $1T'$ -WTe₂ with $n_e = 9.5 \times 10^{13} \text{ cm}^{-2}$. The linewidth of the spectrum $\gamma_{q,\nu}$ is indicated by the weight of the curves. All Q and Q_i phonon modes have $(0.73\pi/a, q_y)$. (b) The phonon density of states of spectrum in (a). (c) The frequency ω_Q of Q mode as a function of carrier concentration of electrons (red ball) and holes (blue star). The inset depicts the evolution of the Q mode with different charge densities. (d) The calculated $\alpha^2 F(\omega)$ and $\lambda(\omega)$ with the same electron-doped density in (a). (e) The calculated $\alpha^2 F(\omega)$ with blue, dark and red for hole-, non-, and electron-doped cases, respectively and $\lambda(\omega)$ for hole- (h), none-, and electron- (e) doping for comparison. The electron- and hole-doped densities correspond to those in Fig.1 (c) and (d), respectively.

(EPC) strength $\lambda(\omega)$ shown in Fig. 2(d) and (e). The details about $\gamma_{q,\nu}$, $\alpha^2 F(\omega)$ [26], and $\lambda(\omega)$ are shown in Section III in SM. With them, one can get a crucial expression for the effective attractive interaction as follows,

$$V_{q,\nu}^{ep} = -4\gamma_{q,\nu}/(\pi N_0^2 \omega_{q,\nu}^2). \quad (1)$$

Here, N_0 is the electronic density of states at the Fermi surface for both spin orientations. From Fig. 2(a), and Fig. S4 (a) and (d) in SM, one can find that some optical modes have large linewidth $\gamma_{q,\nu}$ for all three cases. The relevant frequency $\omega_{q,\nu}$, however, is very high. From Eq. (1), the $V_{q,\nu}^{ep}$ from the optical modes can be neglected. The dramatic difference

occurs for the longitudinal acoustic mode. One can find that the electron doping can greatly enlarge the linewidth $\gamma_{q,\nu}$ and soften the frequency $\omega_{q,\nu}$ at the specific momenta Q and Q_i . Therefore, the $\alpha^2 F(\omega)$ and $\lambda(\omega)$ are strongly enhanced by electron doping, as shown in Figs. 2(d), 2(e) and Fig. S4(c), (f) in SM, and so is $V_{q,\nu}^{ep}$. In terms of superconductivity, only the electrons very close to the Fermi surface need to be considered. Such constraint demands the good nesting condition for the electron-doped Fermi surface in Fig. 1 (d), which can be clarified by the electron susceptibility $\chi(q) = \chi'(q) + i\chi''(q)$ (See Section V in SM for details). The Fermi surface nesting is evaluated by the imaginary part $\chi(q)$, i.e., $\chi''(q)$. In Fig. 3 (a), we plot the pattern of $\chi''(q)$ for electron-doped case with $n_e = 9.5 \times 10^{13} \text{cm}^{-2}$. The nesting wave vector $q_{nest} = (0.73\pi/a, 0)$, which is quite close to horizontal ordinate $\sim 0.73\pi/a$ of all Q and Q_i mode phonons. We also plot the evolution of $Q_\Delta = |q_{nest,x} - 0.73\pi/a|$ as the doping density in Fig. 3 (b) and Fig. S6 in SM. One can find that the best nesting with $Q_\Delta \sim 0$ corresponds to the optimal superconductivity with the highest transition temperature T_c , as shown in Fig. 4 (a). The consistent relationship between the phonon spectrum and the electronic structure indicates that the Fermi surface nesting plays the important role to drive the superconductivity in 1T'-WTe₂.

Furthermore, we calculate the superconducting transition temperature T_c in different doping levels using the McMillan-Allen-Dynes formula [21]. The details are presented in Section VI in SM. The calculated results (data points) of T_c as a function of density of electrons (red ball) and holes (blue star) are plotted in Fig. 4(a). Clearly, compared to the hole doping, the electron doping indeed strengthens the T_c of monolayer 1T'-WTe₂, showing significant asymmetry features. More interestingly, the T_c curve shows two remarkable features. First, the T_c exponentially increases as pumping electrons. The nonlinear behavior of T_c curve is further supported by the exponential decay trend of logarithmic average frequency ω_{\log} and the exponential ascend trend of the EPC constant λ^{ph} , as shown in Fig. S8 in SM. The behavior of T_c curve provides the possibility to obtain the quite high T_c superconductivity through increasing electron doping, which is different from the doped graphene [27] or doped antimonene [28]. Second, T_c reaches the maximum of 3.3 K with $n_e = 9.5 \times 10^{13} \text{cm}^{-2}$ corresponding to the best nesting condition, then drops, and finally disappears or merges into the possible CDW state. Here, we discuss a little more about the CDW instability. Recall that the frequency ω_q of Q mode phonon becomes negative when n_e increases cross $10.3 \times 10^{13} \text{cm}^{-2}$, as shown in Fig. 1(c). It indicates the lattices

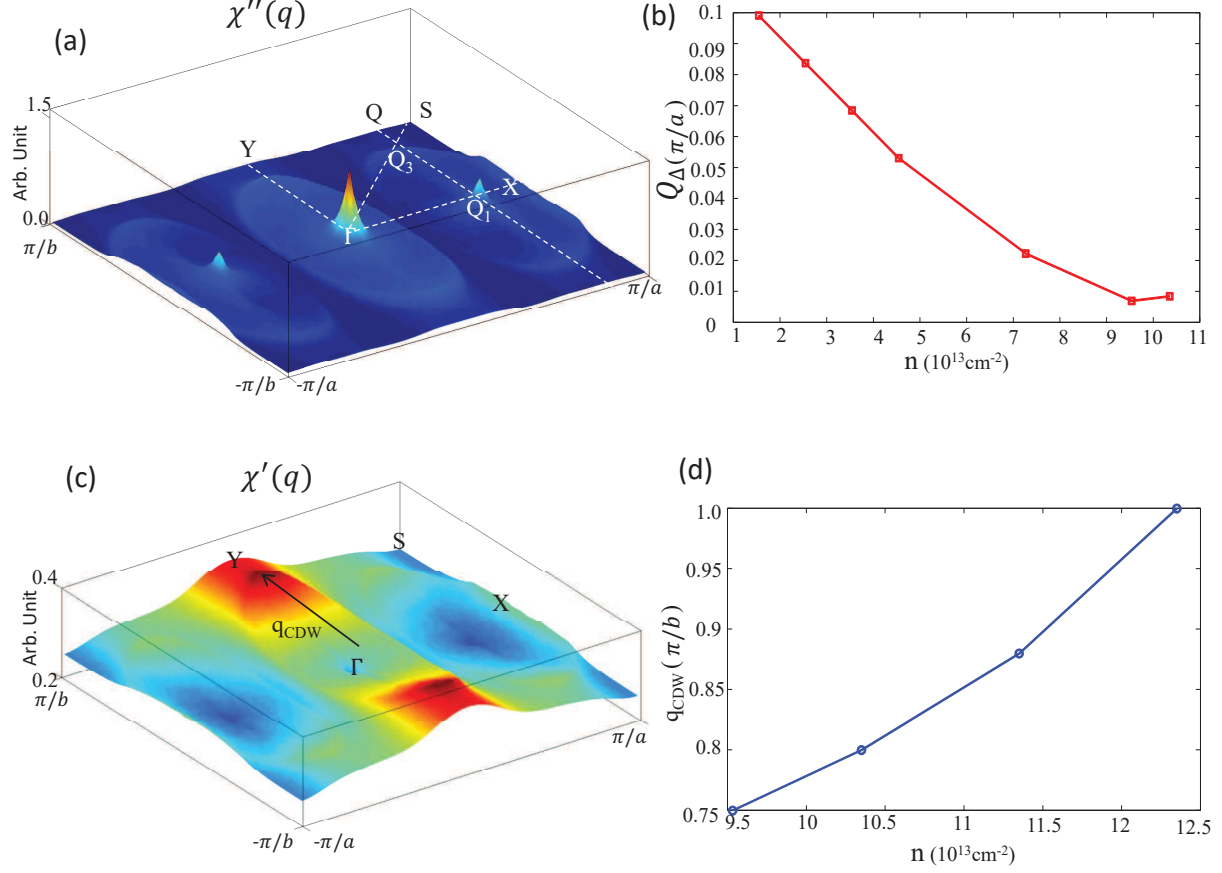


FIG. 3: (Color online)(a) and (c) The imaginary and real electron susceptibility $\chi''(q)$ and $\chi'(q)$ for the electron doping with $n_e = 9.5 \times 10^{13} \text{cm}^{-2}$, respectively. Note that the peak of $\chi''(q=0)$ in (a) is trivial. (b) The evolution of $Q_\Delta = |q_{nest,x} - 0.73\pi/a|$ versus the electron-doped level. (d) The evolution of CDW wave vector versus the electron-doped level.

become unstable and the system undergoes a possible CDW transition. For the electronic states, the CDW instability is induced by the divergence of $\chi'(q)$, the real part of electron susceptibility $\chi(q)$ [29]. In Fig. 3 (c), we plot the pattern of $\chi'(q)$ for electron-doped case with $n_e = 9.5 \times 10^{13} \text{cm}^{-2}$, whose CDW wave vector is $q_{CDW} = (0, 0.75\pi/b)$. When the electron doping increases, q_{CDW} is more and more close to the $(0, \pi/b)$, as shown in Fig. 3(d) and Fig. S7 in SM. We conclude that the CDW with different q_{CDW} should compete with each other, and the most probable one has the wave vector $(0, \pi/b)$, which is quasi-one dimensional, commensurate $2Q$ CDW. Note that the nesting wave vector has nothing to do with the CDW wave vector[29]. According to the above discussions, the relevant phase

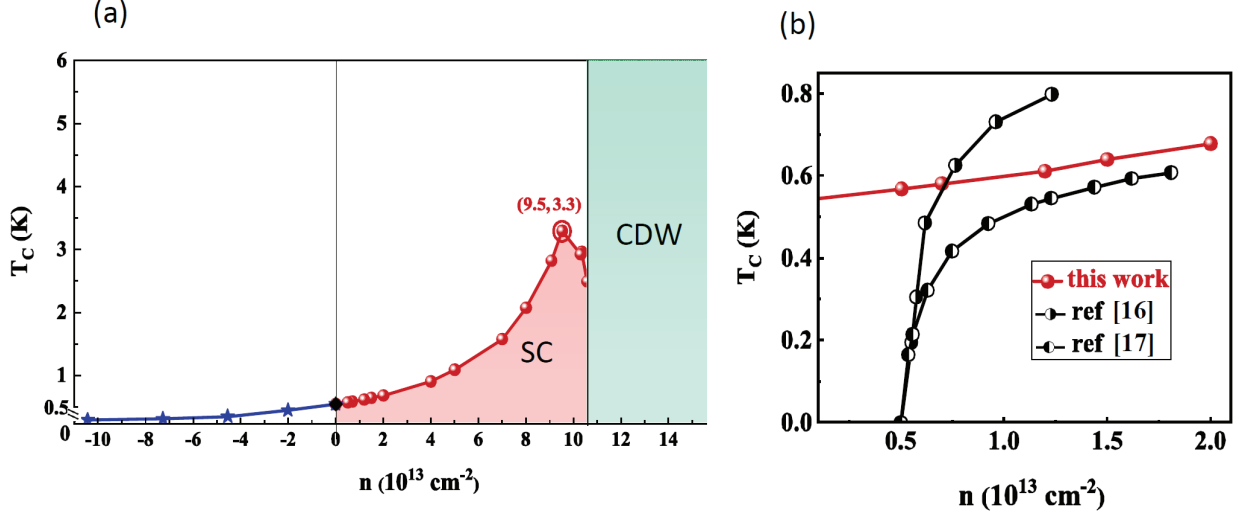


FIG. 4: (Color online) (a) A $T_c - n$ phase diagram is plotted. The boundary of solid line with small balls are given by our calculations. SC and CDW label superconducting phase and charge density wave state, respectively. (b) A comparison between our calculation with the experimental results [16, 17] for e -doped $1T'$ -WTe₂. The logarithmical T_c from [16] has been converted.

diagram can be plotted as shown in Fig. 4 (a), from which a superconducting dome can be found. Currently, using solid-state gates or ionic-liquid gates, typical carrier density (10^{14} cm^{-2}) can be achieved in several two-dimensional (2D) materials [30–34], we thus expect that future experiments for electron-doped $1T'$ -WTe₂ can verify our predicted maximum T_c (3.3 K), which is about four or five times the experimental values of 0.8 K [16] or 0.6 K [17]. In the range of experimental charge density, i.e., $n \in [0.7, 2.1] \times 10^{13} \text{ cm}^{-2}$, our results are in qualitatively agreement with the experimental values [16, 17], as shown in Fig. 4 (b). Whereas T_c greatly deviates from the experimental value below $0.7 \times 10^{13} \text{ cm}^{-2}$. It is because the Coulomb screening effect is strongly reduced in the low density regime. Correspondingly, the constant retarded Coulomb pseudo-potential μ^* is not exact and should become large to reduce T_c from Eq.(7) in SM.

Now, we turn to understand the superconducting properties of monolayer $1T'$ -WTe₂ in the electron-doped regime. According to Fig. 1(d), there exist two separated Fermi pockets centered at momenta \mathbf{K}' and \mathbf{K} which can be regarded as two valleys. The low-energy Hamiltonian can be expanded around \mathbf{K}' and \mathbf{K} . Define the annihilation electron operator as $c_{\mathbf{k},\eta,s}$, where \mathbf{k} is the momentum measured from \mathbf{K}' and \mathbf{K} , $\eta = \pm$ is for two valleys and

TABLE I: Classification of the inter-valley s -wave pairings according to the representations of C_{2h} point group.

	$C_2(z)$	σ_h	i	$\hat{\Delta}$	$\hat{\Delta}$
IR	$s_z\tau_x$	$-is_z$	τ_x	Matrix form	Explicit form
A_g	1	1	1	τ_x	$c_{+\uparrow}c_{-\downarrow} - c_{+\downarrow}c_{-\uparrow}$
B_u	-1	1	-1	$s_z\tau_y$	$c_{+\uparrow}c_{-\downarrow} + c_{+\downarrow}c_{-\uparrow}$
A_u	1	-1	-1	$s_x\tau_y$	$c_{+\uparrow}c_{-\uparrow} - c_{+\downarrow}c_{-\downarrow}$
				$s_y\tau_y$	$i(c_{+\uparrow}c_{-\uparrow} + c_{+\downarrow}c_{-\downarrow})$

$s = \uparrow, \downarrow$ is for spin. On the basis of $[c_{\mathbf{k},+, \uparrow}, c_{\mathbf{k},-, \uparrow}, c_{\mathbf{k},+, \downarrow}, c_{\mathbf{k},-, \downarrow}]$, the effective Hamiltonian is

$$\mathcal{H}_0 = (\varepsilon_k - \mu)s_0\tau_0 + g\mu_B\tau_0\mathbf{B} \cdot \mathbf{s}. \quad (2)$$

Here, s and τ are two sets of Pauli matrices for spin and valley degrees of freedom, $\varepsilon_k = \hbar^2 k^2 / 2m - \mu$ is the dispersion with the chemical potential μ , g and μ_B are the Lande g factor and Bohr magneton, respectively, and $\mathbf{B} = (B_x, B_y, B_z)$ is the external magnetic field. Note that we only take into account the Zeeman effect of the external magnetic field, but neglect the orbital effect due to the 2D feature of 1T'-WTe₂. In the superconducting states, the pairings should follow the IRs of the C_{2h} point group of 1T'-WTe₂. In order to consider the superconductivity for simplicity, we adopt the approximation of Fermi surface average of $V_{q,\nu}^{ep}$ to neglect the weak momentum dependence, *i.e.*, $V^{ep} = \sum_{\nu} \langle V_{\mathbf{k}-\mathbf{k}',\nu}^{ep} \rangle_{\mathbf{k},\mathbf{k}' \in FS}$. Thus, we only consider the momentum-independent s -wave pairings, which are from the constant pairing interaction $-V_0 = V^{ep} + U_{scou}$ with U_{scou} the screened Coulomb interaction. Furthermore, the soft-mode phonons have the momenta connecting the two valleys, which indicates only the inter-valley pairing is possible. Under the mean-field approximation in the Nambu basis, we can classify the pairing symmetry under the constraint of anti-commutation relation between fermion operators. The pairing function can be parameterized by the form $\hat{\Delta} = \sum_i \Delta_i \Gamma_i$, where Γ_i is the i th IR matrix product from s and τ . The results are listed in Table I. More details are shown in Section VII in SM. The pairing interaction in all pairing channels in Table I has the same amplitude of $V_0/2$.

To evaluate the possible superconducting pairing in 1T'-WTe₂, we solve the following linearized gap equations for T_c [35, 36],

$$V_0\chi_i/2 = 1, \quad (3)$$

where χ_i is the finite temperature superconducting susceptibility in i th pairing channel, and can be calculated by

$$\chi_i = -\frac{1}{\beta} \sum_{i\omega_n, k} \text{Tr}[\Gamma_i^\dagger \mathcal{G}_e(k, i\omega_n) \Gamma_i \mathcal{G}_h(k, i\omega_n)]. \quad (4)$$

Here, $\mathcal{G}_{e/h}(k, i\omega_n) = [i\omega_n \mp \mathcal{H}_0(k)]^{-1}$ are the relevant standard electron and hole Matsubara Green functions. The details are shown in Section VII in SM, and we only list the key results here. Note that only the electron-type bands are taken into account in the electron-doped regime. With the approximation that the pairing occurs at the Fermi surface, we can get $\chi_{A_g} = 4\chi_0$, $\chi_{B_u} = 4\chi_0 B_z^2/B^2$, $\chi_{A_u} = 4\chi_0 B_x^2/B^2$ or $4\chi_0 B_y^2/B^2$. $\chi_0 = N_0 \int d\varepsilon \tanh(\frac{\varepsilon}{2k_B T})/\varepsilon$ is the standard superconducting susceptibility and k_B is the Boltzmann constant. When $\mathbf{B} = 0$, one can find that all the pairing channels have the same superconducting susceptibility, i.e., $4\chi_0$, likewise, the same T_c , i.e., $k_B T_c = \frac{2e\gamma}{\pi} \hbar \omega_D \exp(-\frac{1}{2N_0 V_0})$, where $\gamma \approx 0.5772$ is the Euler constant and ω_D is the Debye frequency. It indicates that all the pairing channels are degenerate and are the possible candidate for the superconducting ground state. When $\mathbf{B} \neq 0$, the T_c of A_g channel is robust against the magnetic field. The T_c of B_u or A_u channel is magnetic-field-direction dependent. Namely, $\ln \frac{T_{c,B_u}(B)}{T_{c,B_u}(0)} = \frac{1}{2N_0 V_0} (1 - \frac{B^2}{B_z^2})$ and $\ln \frac{T_{c,A_u}(B)}{T_{c,A_u}(0)} = \frac{1}{2N_0 V_0} (1 - \frac{B^2}{B_{x/y}^2})$. Therefore, the B_u channel is robust against the out-of-plane magnetic field $B = (0, 0, B_z)$ and is fragile for the in-plane magnetic field $B = (B_x, B_y, 0)$. In other words, B_u channel has large $H_{c2,\perp}$ and small $H_{c2,\parallel}$. Similarly, one can find A_u channel has small $H_{c2,\perp}$ and large $H_{c2,\parallel}$. In comparison with the experimental observations, it indicates the superconducting state should fall into the A_u channel with the equal-spin-triplet pairing, whose H_{c2} cannot be restricted by the Pauli paramagnetic limit. These results can be easily understood through the spin structure of the Cooper pairs. The B_u and A_u channels correspond to the three components S_z and S_x, S_y of the $S = 1$ spin-triplet Cooper pairs, respectively. Therefore, the couplings between them and the magnetic field follow the Zeeman-type to minimize the ground state energy. For a general magnetic field with $B = B_0(\cos \theta \cos \varphi, \cos \theta \sin \varphi, \sin \theta)$, we can get the exact pairing form as $\hat{\Delta} \sim e^{i\varphi} c_{\mathbf{k},\uparrow} c_{-\mathbf{k},-\uparrow} - e^{-i\varphi} c_{\mathbf{k},+\downarrow} c_{-\mathbf{k},-\downarrow}$, where the phase φ is determined by the direction of magnetic field.

There exist several other mechanisms to result in the anisotropic H_{c2} including type-I [33, 37, 38], type-II Ising pairings [39] and spin-orbit scattering [40]. Type-I Ising pairing mechanism is related to inversion symmetry breaking and clearly is not the case in monolayer $1T'$ -WTe₂, which preserves the inversion symmetry. Type-II Ising pairing mechanism relies on the band near Γ point with out-of-plane orientation of the spin locked by the spin-orbit coupling. This mechanism can also be excluded, because no such kind of band splitting exists in monolayer $1T'$ -WTe₂. For the spin-orbit scattering mechanism, there are two kinds of situations. In the clean limit of crystalline sample with high mobility, the spin-orbit coupling scattering can be discarded as it could induce the unphysically short scattering times [33, 37, 38]. In the dirty limit, the strong spin-orbit coupling indeed could induce the anisotropic H_{c2} . However, the superconductivity refers to the Fermi surface connected by the momenta relating to soft phonons. From Fig. 1 (a), the pieces of the Fermi surfaces have strong effective spin-orbit coupling is close to Γ point, whereas the pieces of the Fermi surfaces connected by nesting wave vector has weak effective spin-orbit coupling [41]. This is also the reason why the simple low-energy Hamiltonian in Eq. (2) is enough and is adopted to investigate the properties of superconducting state in monolayer $1T'$ -WTe₂. Thus, the spin-orbit scattering mechanism can be excluded.

In conclusion, we have determined the soft-mode phonons, the relevant enhanced electron-phonon coupling and the Fermi surface nesting are three ingredients to drive the superconductivity in electron-doped monolayer $1T'$ -WTe₂. We also predict a quasi-one dimensional commensurate $2Q$ CDW emerges in the heavy electron doping regime, and a superconducting dome in the phase diagram. Furthermore, we propose an unconventional superconducting pairing with equal spin triplet to capture the experimentally observed strong anisotropic upper critical fields. Our studies provide a standard way to understand the gating-dependent superconductivity in $1T'$ -WTe₂ and other transition metal dichalcogenides.

Acknowledgments

This work was financially supported by the National Key R&D Program of China No. 2017YFA0303201, National Natural Science Foundation of China under Grants (No. 11625415, No. 61605014, No. 11674331), the ‘‘Strategic Priority Research Program (B)’’ of the Chinese Academy of Sciences, Grant No. XDB33030100, the ‘100 Talents Project’ of the

Chinese Academy of Sciences, the Collaborative Innovation Program of Hefei Science Center, CAS (Grants No. 2020HSC-CIP002), the CASHIPS Director's Fund (BJPY2019B03), the Science Challenge Project under Grant No. TZ2016001. A portion of this work was supported by the High Magnetic Field Laboratory of Anhui Province, China.

-
- [1] Y. S. Hor, A. J. Williams, J. G. Checkelsky, P. Roushan, J. Seo, Q. Xu, H. W. Zandbergen, A. Yazdani, N. P. Ong, and R. J. Cava, *Phys. Rev. Lett.* **104**, 057001 (2010).
 - [2] Z. Liu, X. Yao, J. Shao, M. Zuo, L. Pi, S. Tan, C. Zhang, and Y. Zhang, *J. Am Chem. Soc.* **137**, 10512 (2015).
 - [3] M. P. Smylie, K. Willa, H. Claus, A. Snezhko, I. Martin, W.-K. Kwok, Y. Qiu, Y. S. Hor, E. Bokari, P. Niraula, A. Kayani, V. Mishra, and U. Welp, *Phys. Rev. B* **96**, 115145 (2017).
 - [4] T. Asaba, B. J. Lawson, C. Tinsman, L. Chen, P. Corbae, G. Li, Y. Qiu, Y. S. Hor, L. Fu, and L. Li, *Phys. Rev. X* **7**, 011009 (2017).
 - [5] K. Kirshenbaum, P. S. Syers, A. P. Hope, N. P. Butch, J. R. Jeffries, S. T. Weir, J. J. Hamlin, M. B. Maple, Y. K. Vohra, and J. Paglione, *Phys. Rev. Lett.* **111**, 087001 (2013).
 - [6] C. Zhang, L. Sun, Z. Chen, X. Zhou, Q. Wu, W. Yi, J. Guo, X. Dong, and Z. Zhao, *Phys. Rev. B* **83**, 140504(R) (2011).
 - [7] L. Fu and C. L. Kane, *Phys. Rev. Lett.* **100**, 096407 (2008).
 - [8] R. M. Lutchyn, J. D. Sau, and S. D. Sarma, *Phys. Rev. Lett.* **105**, 077001 (2010).
 - [9] J. Xu, C. Liu, M. Wang, J. Ge, Z. Liu, X. Yang, Y. Chen, Y. Liu, Z. Xu, C. Gao, D. Qian, F. Zhang, and J. Jia, *Phys. Rev. Lett.* **112**, 217001 (2014).
 - [10] N. Hao and J. Hu, *Natl. Sci. Rev.* **6**, 213 (2019).
 - [11] H. Wang, L. Ma, and J. Wang, *Sci. Bull.* **63**, 1141 (2018).
 - [12] H. Wang, H.-C. Wang, H.-W. Liu, H. Lu, W.-H. Yang, S. Jia, X.-J. Liu, X.-C. Xie, J. Wei, and J. Wang, *Nat. Mater.* **15**, 38 (2016).
 - [13] L. Aggarwal, A. Gaurav, G. S. Thakur, Z. Haque, A. K. Ganguli, and G. Sheet, *Nat. Mater.* **15**, 32 (2016).
 - [14] X.-Y. Hou, Z. Wang, Y.-D. Gu, J.-B. He, D. Chen, W.-L. Zhu, M.-D. Zhang, F. Zhang, Y.-F. Xu, S. Zhang, H.-X. Yang, Z.-A. Ren, H.-M. Weng, N. Hao, W.-G. Lv, J.-P. Hu, G.-F. Chen, and L. Shan, *Phys. Rev. B* **100**, 235109 (2019).

- [15] X.-Y. Hou, Y.-D. Gu, S.-J. Li, L.-X. Zhao, W.-L. Zhu, Z. Wang, M.-D. Zhang, F. Zhang, L. Zhang, H. Zi, Y.-W. Wu, H.-X. Yang, Z.-A. Ren, P. Zhang, G.-F. Chen, N. Hao, and L. Shan, Phys. Rev. B **101**, 134503 (2020).
- [16] E. Sajadi, T. Palomaki, Z. Fei, W. Zhao, P. Bement, C. Olsen, S. Luescher, X. D. Xu, J. A. Folk and D. H. Cobden, Science **362**, 922 (2018).
- [17] V. Fatemi, S. F. Wu, Y. Cao, L. Bretheau, Q. D. Gibson, K. Watanabe, T. Taniguchi, T. J. Cava, and P. Jarillo-Herrero, Science **362**, 926 (2018).
- [18] J. P. Perdew and A. Zunger, Phys. Rev. B **23**, 5048 (1981).
- [19] D. M. Ceperley and B. J. Alder, Phys. Rev. Lett. **45**, 566 (1980).
- [20] P. Giannozzi et al., J. Phys. Condens. Matter **21**, 395502 (2009).
- [21] P. B. Allen and R. Dynes, Phys. Rev. B **12**, 905 (1975).
- [22] See Supplemental Material at [<http://rui>] for details on the calculation method, electronic state calculation, phonon spectrum calculation, electron-phonon coupling calculation, atom vibration calculation, the T_c calculation, the symmetry classification and the linearized gap function for the superconducting pairing, which includes Refs. [23–24].
- [23] Y. Wang, J. Xiao, H. Zhu, Y. Li, Y. Alsaïd, K. Y. Fong, Y. Zhou, S. Wang, W. Shi, Y. Wang, A. Zettl, E. J. Reed and X. Zhang, Nature **550**, 487 (2017).
- [24] L. Wang, W. Wang and X. Bai, J. Am. Chem. Soc. **136**, 6693 (2014).
- [25] W. Yang, Z. Y. Yuan, Y. Q. Luo, Y. Yang, F. W. Zheng, Z. H. Hu, X. H. Wang, Y. A. Liu, and P. Zhang, Phys. Rev. B **99**, 235401 (2019).
- [26] P. B. Allen, Phys. Rev. B **6**, 2577 (1972).
- [27] C. Si, Z. Liu, W. H. Duan, and F. Liu, Phys. Rev. Lett. **111**, 196802 (2013).
- [28] A. V. Lugovskoi, M. I. Katsnelson, and A. N. Rudenko, Phys. Rev. B **99**, 064513 (2019).
- [29] M. D. Johannes and I. I. Mazin, Phys. Rev. B **77**, 165135 (2008).
- [30] Y. J. Fu, E. Liu, H. T. Yuan, P. Z. Tang, B. Lian, G. Xu, J. W. Zeng, Z. Y. Chen, Y. J. Wang, W. Zhou, K. Xu, A. Y. Gao, C. Pan, M. Wang, B. G. Wang, S. C. Zhang, Y. Cui, H. Y. Hwang, and F. Miao, NPJ Quantum Mater. **2**, 52 (2017).
- [31] L. J. Li, E. C. T. O’Farrell, K. P. Loh, G. Eda, B. Öyilmaz, and A. H. Castro neto, Nature **529**, 185 (2016).
- [32] Y. Saito, T. Nojima, and Y. Iwasa, Supercond. Sci. Tech. **29**, 093001 (2016).
- [33] J. M. Lu, O. Zheliuk, I. Leermakers, N. F. Q. Yuan, U. Zeitler, K. T. Law, and J. T. Ye,

- Science **350**, 1353 (2015).
- [34] D. Costanzo, S. Jo, H. Berger, and A. F. Morpurgo, Nat. Nanotech. **11**, 339 (2016).
 - [35] L. Fu and E. Berg, Phys. Rev. Lett. **105**, 097001 (2010).
 - [36] C. Liu, Phys. Rev. Lett. **118**, 087001 (2010).
 - [37] Y. Saito, Y. Nakamura, M. S. Bahramy, Y. Kohama, J. Ye, Y. Kasahara, Y. Nakagawa, M. Onga, M. Tokunaga, T. Nojima, Y. Yanase, and Y. Iwasa, Nat. Phys. **12**, 144–149 (2016).
 - [38] X. Xi, Z. Wang, W. Zhao, J. Park, K. T. Law, H. Berger, L. Forró, J. Shan, and K. F. Mak, Nat. Phys. **12**, 139–143 (2016).
 - [39] J. Falson, Y. Xu, M. Liao, Y. Zang, K. Zhu, C. Wang, Z. Zhang, H. Liu, W. Duan, K. He, H. Liu, J. H. Smet, D. Zhang, and Q.-K. Xue, Science, aax3873 (2020).
 - [40] R. A. Klemm, A. Luther, and M. R. Beasley, Phys. Rev. B **12**, 877 (1975).
 - [41] X. Qian, J. Liu, L. Fu, and J. Li, Science **346**, 1344 (2014).